

η and η' mesons from $N_f = 2 + 1$ lattice QCD at the physical point using topological charge operators

Yue Su,¹ Nan Wang,^{2,3,4} Long-cheng Gui,^{5,6,7,*} Jun Hua,^{2,4} Jian Liang,^{2,4,†} and Jun Shi^{2,4,‡}

¹Center for Joint Quantum Studies and Department of Physics,
School of Science, Tianjin University, Tianjin 300350, China

²State Key Laboratory of Nuclear Physics and Technology, Institute of Quantum Matter,
South China Normal University, Guangzhou 510006, China

³Key Laboratory of Atomic and Subatomic Structure and Quantum Control (MOE),
Guangdong-Hong Kong Joint Laboratory of Quantum Matter, Guangzhou 510006, China

⁴Guangdong Basic Research Center of Excellence for Structure and Fundamental Interactions of Matter,
Guangdong Provincial Key Laboratory of Nuclear Science, Guangzhou 510006, China

⁵Department of Physics, Hunan Normal University, Changsha 410081, China

⁶Synergetic Innovation Center for Quantum Effects and Applications (SICQEA), Changsha 410081, China

⁷Key Laboratory of Low-Dimensional Quantum Structures and Quantum Control of Ministry of Education, Changsha 410081, China



(χ QCD Collaboration)

By fitting the two-point correlation functions of topological charge density operators calculated on two $2 + 1$ -flavor gauge ensembles with physical pion mass, we determine both the η and η' masses and also the mixing angle to be $m_\eta = 0.522(27)(22)$ GeV, $m_{\eta'} = 0.970(56)(17)$ GeV, and $\theta_1 = -10.7(1.4)(0.2)^\circ$, respectively, where the first error is the statistical uncertainty and the second one is the systematic uncertainty of lattice discretization effects. This is the first extraction of both η/η' masses and the mixing angle θ_1 using topological charge operators. Compared with previous studies using quark bilinear operators, the error of the η mass is relatively large, but the mixing angle has remarkably high precision. This demonstrates that the topological charge operators are well suited to study the η and η' mesons.

I. INTRODUCTION

Understanding the masses of η and η' mesons as well as the mixing between the original flavor singlet state η_1 and the neutral octet state η_8 is an important topic in low-energy strong-interaction physics. In one respect, the spontaneous breaking of the chiral symmetry results in the mass of the Goldstone bosons. Also, through the partially conserved axial current (PCAC) relation, the pseudoscalar current is modified by the non-trivial topological structure of the gauge fields, and the mass of the flavor-singlet pseudoscalar particle is significantly heavier than that of the other pseudoscalar particles due to the $U_A(1)$ anomaly. In another respect, the mixing angle between the flavor singlet and octet states is a direct measurement of the breaking of $SU(3)$ flavor symmetry [1–3].

Due to the flavor-singlet components, lattice calculations of η and η' mesons using quark bilinear interpolating field operators involve disconnected insertions, which require high statistics. Though challenging, many efforts with this method have been made in the community on the η and η' masses, from quenched approximations [4, 5] to dynamical fermions with $N_f = 2$ [6–9], $N_f = 2 + 1$ [10–14], and $N_f = 2 + 1 + 1$ [15, 16]. Moreover, the study [10] reports the first realistic calculation of the octet-singlet mixing angle and confirms that the

large mass of η' arises from the combined effects of the axial anomaly and the gauge field topology in QCD. A recent work [13] provides detailed calculations and analysis on this topic with gauge ensembles of different parameters, including one with the physical pion mass.

The ingenious calculation of η' mass using operators of the topological charge density was carried out in 2015 on a $2+1$ -flavor lattice at one single lattice spacing and with an unphysical pion mass [17]. This approach avoids the difficulties of handling disconnected insertions. A follow-up work [18] performs similar calculations of the η' meson mass on several $N_f = 2$ flavor gauge ensembles with one at the physical pion mass.

For now, there still lacks a comprehensive lattice calculation of both η and η' masses and also the mixing angle using the interpolating operators of topological charge density. Such a study provides insights into the nature of η and η' mesons, and also the physics of axial anomaly and gauge field topology. The results can be compared with those obtained using quark bilinear operators. In this article, we report our calculations of the masses of the η and η' mesons as well as the singlet-octet mixing angle θ_1 using topological charge density operators on two $2 + 1$ -flavor gauge ensembles both at the physical point with different lattice spacings. A simple continuum limit is taken and the systematic uncertainties in the data analysis are carefully considered.

This paper is organized as follows: In Sec. II, we describe our lattice setup and discuss the two-point correlation functions of the topological charge density operators. Sec. III

* guilongcheng@hunnu.edu.cn

† jianliang@sclu.edu.cn

‡ jun.shi@sclu.edu.cn

Symbol	$L^3 \times T$	a (fm)	m_K (MeV)	m_π (MeV)	N_{cfg}
48I	$48^3 \times 96$	0.1141(2)	499	139	356
64I	$64^3 \times 128$	0.0837(2)	508	139	330

TABLE I. Parameters of the gauge ensembles including the numbers of the configurations N_{cfg} used in this study.

presents the details of data analysis on the η and η' masses and the mixing angle. Some discussion and a summary are provided in Sec. IV.

II. NUMERICAL DETAILS

We employ two 2 + 1-flavor gauge ensembles of domain wall fermions generated by the RBC/UKQCD collaboration [19]. Both of them are at the physical pion mass point. We have two different lattice spacings, and the discretization effects of our results are carefully estimated. Detailed parameters of the gauge ensembles are collected in Table I.

As stated in the introduction, in this work, we extract the masses of the η and η' mesons and the corresponding mixing parameter from calculating the correlation functions of topological charge density operators. The topological charge is actually the scalar product of the color electric and magnetic fields and carries a quantum number same as η and η' , i.e., 0^+0^{-+} . We use the Symanzik improved version of the topological charge density to reduce the discretization errors [20],

$$q(x) = c_0 q^{\text{clov}}(x) + c_1 q^{\text{rect}}(x), \quad (1)$$

where $c_0 = 5/3$ and $c_1 = -1/12$ are the tree-level Symanzik coefficients, and $q^{\text{clov}}(x)$ and $q^{\text{rect}}(x)$ are defined from the corresponding field tensor $F_{\mu\nu}^{\text{clov (rect)}}(x)$ as

$$q(x)^{\text{clov (rect)}} = \frac{1}{32\pi^2} \epsilon_{\mu\nu\rho\sigma} \text{Tr} \{ F_{\mu\nu}^{\text{clov (rect)}}(x) F_{\rho\sigma}^{\text{clov (rect)}}(x) \}. \quad (2)$$

The Wilson loops used to construct the field tensors are illustrated in Fig. 1. $F_{\mu\nu}^{\text{clov}}(x)$ represents the ordinary clover leaf construction, while $F_{\mu\nu}^{\text{rect}}(x)$ is from the sum of the horizontally and vertically oriented rectangular Wilson loops depicted by the second and third diagrams of Fig. 1.

The Euclidean correlation functions of topological charge density operators are expressed as

$$C_2(r) = \langle q(x) q(y) \rangle, \quad (3)$$

where x and y are spacetime coordinates and $r = |x - y|$ is a 4-D distance. The reason we calculate the 4-D correlation of the topological charge operators rather than the common temporal correlation lies in the behavior of the correlation functions. As shown in Fig. 2, the two-point correlation function has a positive kernel at small r and changes its sign with increasing r . Actually, in the continuum, the reflection positivity and the fact that the topological charge is reflection-odd ensure that the topological charge correlation functions are negative at non-zero distance, and the positive contact contribution is a delta function at $|x - y| = 0$. However, the topological charges

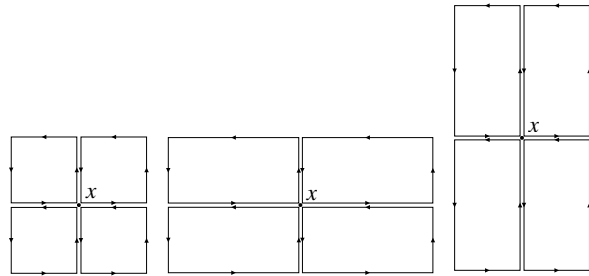


FIG. 1. From left to right, the Wilson loops used to define the clover field tensor $F_{\mu\nu}^{\text{clov}}$, and the horizontal and vertical ones to define the rectangular field tensor $F_{\mu\nu}^{\text{rect}}$. The latter Wilson loops are of sizes 2×1 and 1×2 .

are not locally defined on the lattice, the positive contact contribution is smeared to cover several lattice spacings [21, 22]. Therefore, in order to reliably extract the physical states, one needs to skip the first several lattice spacings and use only the data points of the negative tail. In such a situation, calculating the 4-D distance provides more usable data points, which is also a common choice in previous studies [17, 18].

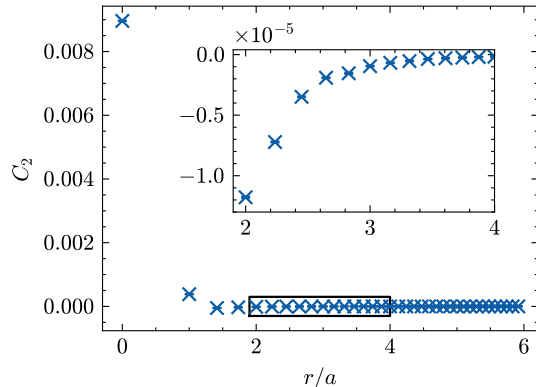


FIG. 2. The two-point correlation function of the topological charge density operator $C_2(r)$ as a function of r on the 48I ensemble. The zoomed in figure shows the negative correlation at large r .

Since we are considering 4-D distances, we have many data points at very close r when r is large. These data points can be strongly correlated and result in difficulties in the numerical analysis. Therefore, we perform a binning procedure: we average the data points in each interval of $\delta_r = 0.5a$ in r as a binned data point. The distance after binning is denoted as $\hat{r} = (0.25 + i \times 0.5)a$ for the i -th interval.

To improve the statistical signal-to-noise ratio, we use Wilson flow [23, 24] to smear our gauge fields. For a flow time t_f , this process creates effectively a smearing radius of $\sqrt{8t_f}$. The application of Wilson flow results in the suppression of the short-range fluctuations and statistical noises [25]. Fig. 3 displays the topological charge density correlator ($-C(r)$ actually for better readability) on the 64I ensemble at different flow times $t_f/a^2 = 1.2, 1.5, 1.8, 2.1$ and 2.4 . Since for large \hat{r} , the correlators of different flow times overlap with each other,

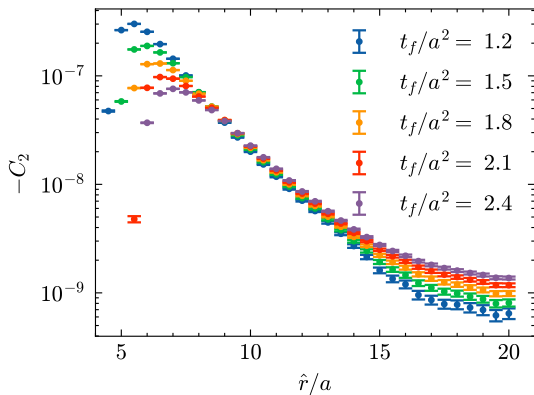


FIG. 3. The correlation functions of topological charge density operators on the 64I ensembles. Additional minus sign is included and the data points with different flow times are shifted vertically for clarity.

we shift the data points vertically for clarity. It is evident that, as the flow time t_f increases, the signal-to-noise ratios at large r get improved. However, in the meanwhile, the contact contribution is further smeared and one has fewer data points left to use. Thus, as a compromise, we find $t_f/a^2=2.4$ is a good choice. In fact, the errors at $t_f/a^2=2.1$ and $t_f/a^2=2.4$ are quite close, and the numerical results extracted from different flow times are all consistent within errors. For the 48I lattice, the optimal flow time we find is $t_f/a^2=1.6$. The difference stems from their different lattice spacings.

III. FITTINGS AND RESULTS

According to the form of the scalar propagator in coordinate space with space-like separation, the correlation functions of topological charge density operators can be expressed as

$$C_2(\hat{r}) = \sum_n A_n \frac{m_n}{\hat{r}} K_1(m_n \hat{r}), \quad (4)$$

where K_1 is the modified Bessel function of the second kind and the summation runs over all the states with 0^+0^- quantum number. In the practical calculations, we use the asymptotic expansion of $K_1(z) = \sqrt{\frac{\pi}{2z}} e^{-z} \left(1 + \frac{3}{8z}\right)$. In the range of z we consider, the difference is around or less than one percent, so the precision is enough for this study.

To have qualitative information of the spectrum, we first extract the effective mass from the correlation functions. The effective mass at each \hat{r} is obtained by solving the following equation numerically

$$\frac{K_1(m_{\text{eff}} \hat{r})}{K_1(m_{\text{eff}}(\hat{r} - \delta_r))} \frac{\hat{r} - \delta_r}{\hat{r}} = \frac{C_2(\hat{r})}{C_2(\hat{r} - \delta_r)}. \quad (5)$$

The results are shown in Fig. 4. One finds that, when \hat{r} is larger than ~ 1.4 fm, the effective masses of both lattices are close to the η mass. And in the middle \hat{r} region, the effective masses

are close to the η' mass. For very small \hat{r} , unphysical contributions due to the positive kernel appear. These observations demonstrate that the correlation functions indeed contain information from both η and η' states. Moreover, they inspired an approach to extract the information: first perform single-state fits in the large \hat{r} region to determine the mass and spectral weight of the ground-state η and then apply constrained two-state fits in the intermediate \hat{r} region to fix the excited-state η' 's parameters. Details are described in the following subsections.

A. fits for the η state

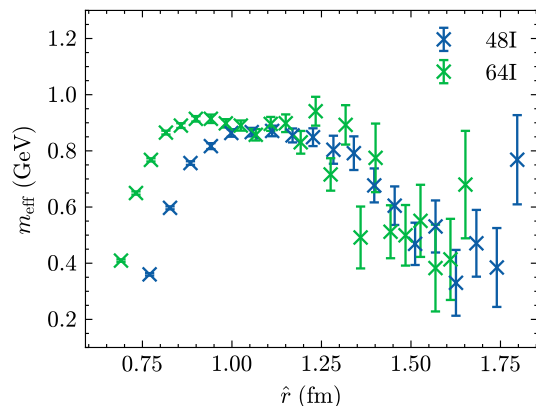


FIG. 4. The effective mass of 48I and 64I ensemble.

We use the single-state version of Eq. (4) to fit for the η state. The fitting results as a function of different starting points \hat{r}_{start} together with the corresponding $\chi^2/\text{d.o.f.}$ are depicted in Fig. 5 and Fig. 6. The end points of the fits are fixed to be $19.25a$ and $15.75a$ for the 64I and 48I ensembles respectively, where the signal is overwhelmed by noise. We identify that the results saturate at $\hat{r}_{\text{start}}/a = 15.75$ for the 64I lattice and $\hat{r}_{\text{start}}/a = 11.75$ for the 48I lattice (green bands in the figures). The $\chi^2/\text{d.o.f.}$ in each case is less than one and, by checking the fitting results of next \hat{r}_{start} (yellow bands in the figures), we confirm that the corresponding systematic uncertainties are subdominant to statistical ones.

The resulting η mass is $0.544(53)$ GeV on the 64I lattice and $0.514(31)$ GeV on the 48I lattice. Since these two values are consistent within errors, we conclude that, within the current statistical precision, no significant discretization errors are observed. This finding is consistent with our earlier results using chiral fermions, e.g., Ref. [26]. Therefore, we determine our final prediction as a constant fit of the results from the two lattices. Furthermore, we take the difference between the constant-fit result and the value obtained on the finer lattice as the systematic uncertainty. In the end, we get $m_\eta = 0.522(27)(22)$ GeV, which is consistent with the experimental value of $547.862(17)$ MeV [27]. More detailed comparison are collected in Fig. 11.

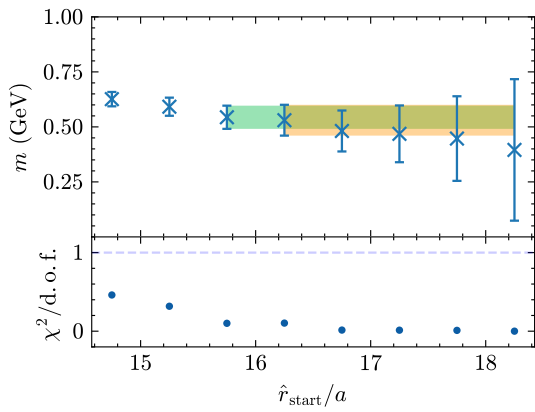


FIG. 5. Single-state fitting results for the η mass on the 64I ensemble as a function of the fitting starting point \hat{r}_{start} . The corresponding $\chi^2/\text{d.o.f.}$ are also presented. The bands are not fitting results, but are used to show more clearly the difference of the fitting results between different \hat{r}_{start} .

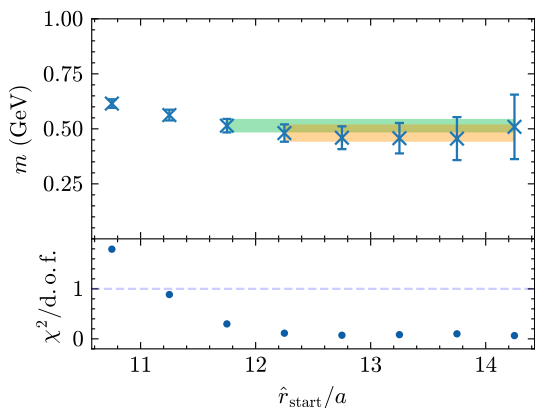


FIG. 6. The same as Fig. 5 but for the 48I ensemble.

B. fits for the η' state

We use Eq. (4) with two states to fit for the η' state

$$C_2(t) = A_{\eta'} \frac{m_{\eta'}}{\hat{r}} K_1(m_{\eta'} \hat{r}) + A_{\eta} \frac{m_{\eta}}{\hat{r}} K_1(m_{\eta} \hat{r}). \quad (6)$$

To make the fits more stable, the previously fitted results of η mass are used as priors in these two-state fits. The spectral weight factor A_{η} is free of prior since the A_{η} 's from the single-state fits are not as reliable as the masses. *N.B.*: In Bayesian statistics, the prior should be independent of the evidence. Therefore, we use different data points in the η' fitting. Specifically, the end points of the η' fittings are fixed to be $15.25a$ and $11.25a$ for the 64I and 48I ensembles respectively, which are actually the preceding points of the starting points in the fits of η .

Similarly, the fitting results as a function of different starting points \hat{r}_{start} together with the corresponding $\chi^2/\text{d.o.f.}$ are depicted in Fig. 7 and Fig. 8. The results saturate at $\hat{r}_{\text{start}}/a = 10.25$ for the 64I lattice and $\hat{r}_{\text{start}}/a = 8.25$ for the 48I lat-

tice (green bands in the figures). Again, the $\chi^2/\text{d.o.f.}$ in each case is less than one. By comparing the green and yellow bands, we find that the systematic uncertainties resulting from different fitting ranges are subdominant to statistical ones and thus are not included in the final results. The η' mass we obtained is $m_{\eta'} = 0.987(65)$ GeV on the 64I lattice and $m_{\eta'} = 0.92(11)$ GeV on the 48I lattice, respectively. Following the same argument and strategy for the η case, our final prediction is $m_{\eta'} = 0.970(56)(17)$ GeV with the second error being the systematic uncertainty of lattice discretization effects, which is reasonably consistent with the physical value $957.78(6)$ MeV [27].

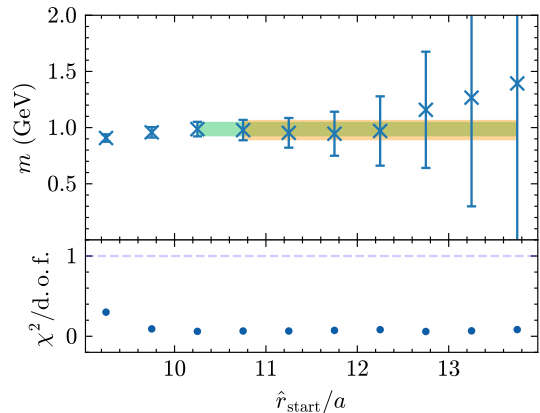


FIG. 7. Two-state fitting results for the η' mass on the 64I ensemble as a function of the fitting starting point \hat{r}_{start} . The corresponding $\chi^2/\text{d.o.f.}$ are also presented. The bands are not fitting results, but are used to show more clearly the difference of the fitting results between different \hat{r}_{start} .

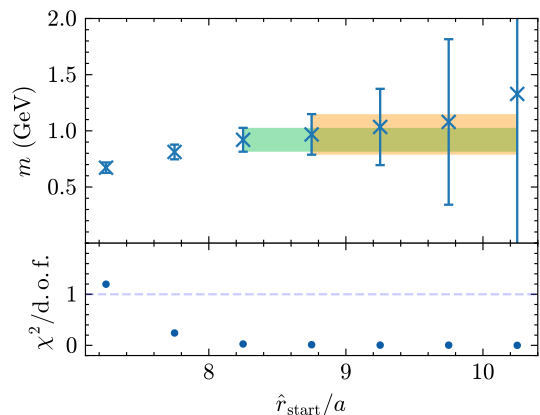


FIG. 8. The same as Fig. 7 but for the 48I ensemble.

C. mixing angle

The mixing of SU(3) singlet state η_1 and the neutral octet state η_8 due to the breaking of the flavor symmetry results in

the physical states η and η' . The corresponding mixing angles measure such mixing. The traditional single-angle mixing scheme is actually a leading-order form, while modern treatment is based on the parametrization of the matrix elements with two mixing angles as [28]

$$\begin{cases} F_{\eta}^8 = F^8 \cos \theta_8 \\ F_{\eta'}^8 = F^8 \sin \theta_8 \\ F_{\eta}^1 = -F^1 \sin \theta_1 \\ F_{\eta'}^1 = F^1 \cos \theta_1 \end{cases}, \quad (7)$$

where $F_{\eta}^8 = \langle 0|O_8|\eta\rangle$, $F_{\eta'}^8 = \langle 0|O_8|\eta'\rangle$, $F_{\eta}^1 = \langle 0|O_1|\eta\rangle$, and $F_{\eta'}^1 = \langle 0|O_1|\eta'\rangle$ with O_8 and O_1 being the flavor octet and singlet current operators, respectively. In the two-state fits, the spectral weight factors are related to the matrix elements

$$\begin{aligned} A_{\eta} &= |\langle 0|O_1|\eta\rangle|^2, \\ A_{\eta'} &= |\langle 0|O_1|\eta'\rangle|^2, \end{aligned} \quad (8)$$

since the topological charge density operator is flavor singlet and in our case $O_1 = q$. Therefore, we have

$$\theta_1 = -\arctan \sqrt{\frac{A_{\eta}}{A_{\eta'}}}. \quad (9)$$

The numerical results of mixing angle θ_1 as a function of fitting start points \hat{r}_{start} are plotted in Fig. 9 and Fig. 10 for the two ensembles we use. The data points we pick are marked as orange in the figures. Analogously, the systematic uncertainties due to different fitting ranges are negligible compared to the statistical ones since the results are quite stable w.r.t. \hat{r}_{start} for both ensembles.

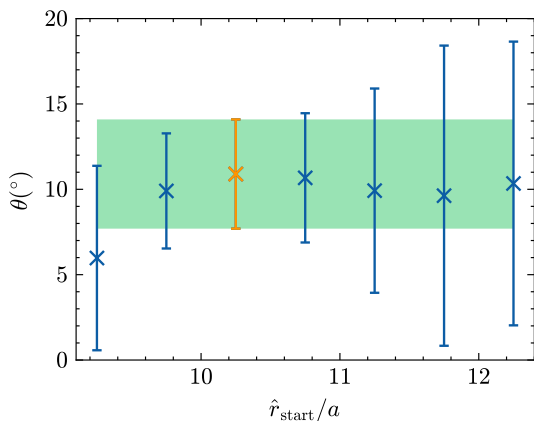


FIG. 9. Results for θ_1 on the 64I ensemble as a function of the fitting starting point \hat{r}_{start} . The orange point is the one we pick for our reported results. The band is not fitting result, but are used to show the consistency between the picked result and the results of other \hat{r}_{start} .

We determine $\theta_1 = -10.9(3.2)^\circ$ on the 64I lattice and $\theta_1 = -10.6(1.6)^\circ$ on the 48I lattice. Still, we use a constant fit for the final prediction and take the difference between the constant-fit result and the value obtained on the finer lattice as the systematic uncertainty of lattice discretization. Our final prediction reads $\theta_1 = -10.7(1.4)(0.2)^\circ$. Since this study uses the topological charge operators, only θ_1 can be determined.

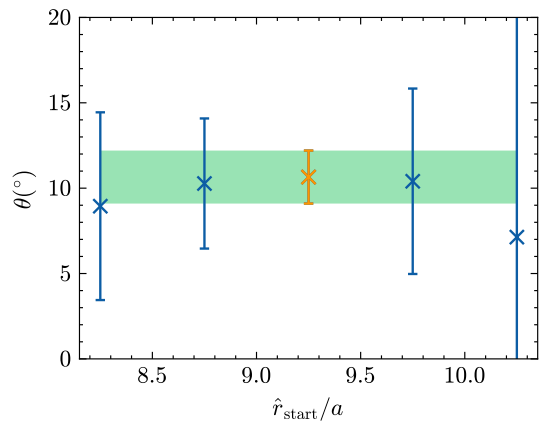


FIG. 10. The same as Fig. 9 but for the the 48I lattice.

IV. SUMMARY AND DISCUSSION

A comparison with other lattice results is summarized in Fig. 11 regarding the η and η' masses and the mixing angle θ_1 . Since some works only reported the mixing angle ϕ in the light-strange flavor basis, we convert ϕ to θ_1 as

$$\theta_1 = \phi - \arctan \left(\frac{\sqrt{2}F_l}{F_s} \right), \quad (10)$$

where F_l and F_s are related to the decay constants of η and η' with light and strange quark axial vector currents, respectively. In Fig. 11, the blue and yellow points represent the results using the topological charge operators and the quark bilinear operators, respectively.

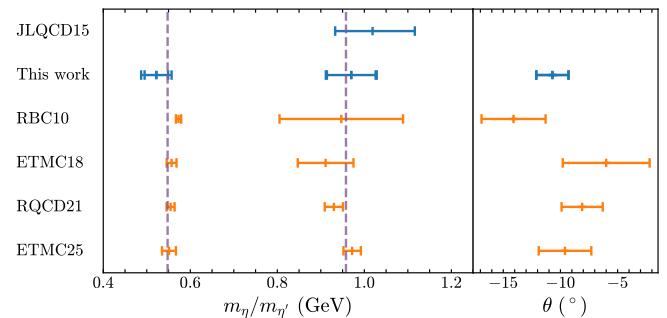


FIG. 11. Comparison of the η and η' masses and the mixing angles from different lattice calculations. The purple vertical dashed lines represent the PDG [27] values of m_{η} and $m_{\eta'}$. We collect the results from JLQCD15 [17], RBC10 [10], ETMC18 [15], RQCD21 [13], and ETMC25 [16], which used $N_f = 2+1$ or $N_f = 2+1+1$ -flavor gauge ensembles and reported both the masses and mixing angles (except for the JLQCD15 study). The blue and yellow colors represent the results using the topological charge operator and the quark bilinear operators, respectively. Some works only reported the mixing angle ϕ in the light-strange flavor basis, and the values of θ_1 quoted here are converted using Eq. 10.

This work, for the first time, extracts both the η and η' masses and also the mixing angle θ_1 by using topological

charge operators. We obtain $m_\eta = 0.522(27)(22)$ GeV, $m_{\eta'} = 0.970(56)(17)$ GeV, and $\theta_1 = -10.7(1.4)(0.2)^\circ$, where the first error is the statistical error and the second one is the systematic error of lattice discretization effects. Compared with the studies using quark operators, the error of the η mass is larger, but the mixing angle has notably high precision. This can be understood by noticing the fact that the topological charge operator is a flavor singlet operator which couples primarily to the η' state ($\left|\frac{A_\eta}{A_{\eta'}}\right| = \tan^2 \theta_1 \sim 0.036$), and one needs to go to very large \hat{r} to reach the ground state η . However, since using topological charge operators avoids the calculations of quark propagators, it offers special advantages for studying the η and η' mesons. Future calculations using more gauge configurations are promising to achieve greater precision than using quark operators.

In addition, the possibility of using a pure-gauge operator to create normal meson states demonstrates that the structure or nature of a hadron state cannot be directly inferred from the creation operators' characteristics; only the quantum numbers

matter.

ACKNOWLEDGEMENT

We thank the RBC/UKQCD collaboration for sharing their DWF gauge configurations. We thank Prof. Ying Chen for valuable discussions. The numerical calculations are performed using the GWU code [29, 30] on the Southern Nuclear Science Computing Center (SNSC) and the Xiangjiang-1 cluster at Hunan Normal University (Changsha). This work is supported by the National Natural Science Foundation of China (NSFC) under Grant Nos. 12175073, 1222503, 12175063, 12105108, and 12205106. J. L. also acknowledges the support of the Natural Science Foundation of Basic and Applied Basic Research of Guangdong Province under Grant No. 2023A1515012712. L. C. Gui is also supported by the Hunan Provincial Natural Science Foundation No. 2023JJ30380 and the Hunan Provincial Department of Education under Grant No.20A310.

-
- [1] S. Weinberg, *Phys. Rev. D* **11**, 3583 (1975).
- [2] A. A. Belavin, A. M. Polyakov, A. S. Schwartz, and Y. S. Tyupkin, *Phys. Lett. B* **59**, 85 (1975).
- [3] E. Witten, *Nucl. Phys. B* **156**, 269 (1979).
- [4] Y. Kuramashi, M. Fukugita, H. Mino, M. Okawa, and A. Ukawa, *Phys. Rev. Lett.* **72**, 3448 (1994).
- [5] L. Venkataraman and G. Kilcup, (1997), [arXiv:hep-lat/9711006](#).
- [6] C. McNeile and C. Michael (UKQCD), *Phys. Lett. B* **491**, 123 (2000), [Erratum: *Phys.Lett.B* 551, 391–391 (2003)], [arXiv:hep-lat/0006020](#).
- [7] K. Hashimoto and T. Izubuchi, *Prog. Theor. Phys.* **119**, 599 (2008), [arXiv:0803.0186 \[hep-lat\]](#).
- [8] K. Jansen, C. Michael, and C. Urbach (ETM), *Eur. Phys. J. C* **58**, 261 (2008), [arXiv:0804.3871 \[hep-lat\]](#).
- [9] X. Jiang, W. Sun, F. Chen, Y. Chen, M. Gong, Z. Liu, and R. Zhang, *Phys. Rev. D* **107**, 094510 (2023), [arXiv:2205.12541 \[hep-lat\]](#).
- [10] N. H. Christ, C. Dawson, T. Izubuchi, C. Jung, Q. Liu, R. D. Mawhinney, C. T. Sachrajda, A. Soni, and R. Zhou, *Phys. Rev. Lett.* **105**, 241601 (2010), [arXiv:1002.2999 \[hep-lat\]](#).
- [11] J. J. Dudek, R. G. Edwards, B. Joo, M. J. Peardon, D. G. Richards, and C. E. Thomas, *Phys. Rev. D* **83**, 111502 (2011), [arXiv:1102.4299 \[hep-lat\]](#).
- [12] E. B. Gregory, A. C. Irving, C. M. Richards, and C. McNeile (UKQCD), *Phys. Rev. D* **86**, 014504 (2012), [arXiv:1112.4384 \[hep-lat\]](#).
- [13] G. S. Bali, V. Braun, S. Collins, A. Schäfer, and J. Simeth (RQCD), *JHEP* **08**, 137, [arXiv:2106.05398 \[hep-lat\]](#).
- [14] Z. R. Kordov *et al.* (CSSM/QCDSF/UKQCD), *Phys. Rev. D* **104**, 114514 (2021), [arXiv:2110.11533 \[hep-lat\]](#).
- [15] K. Ottnad and C. Urbach (ETM), *Phys. Rev. D* **97**, 054508 (2018), [arXiv:1710.07986 \[hep-lat\]](#).
- [16] K. Ottnad, S. Bacchio, J. Finkenrath, B. Kostrzewa, M. Petschlies, F. Pittler, C. Urbach, and U. Wenger, (2025), [arXiv:2503.09895 \[hep-lat\]](#).
- [17] H. Fukaya, S. Aoki, G. Cossu, S. Hashimoto, T. Kaneko, and J. Noaki (JLQCD), *Phys. Rev. D* **92**, 111501 (2015), [arXiv:1509.00944 \[hep-lat\]](#).
- [18] P. Dimopoulos *et al.*, *Phys. Rev. D* **99**, 034511 (2019), [arXiv:1812.08787 \[hep-lat\]](#).
- [19] T. Blum *et al.* (RBC, UKQCD), *Phys. Rev. D* **93**, 074505 (2016), [arXiv:1411.7017 \[hep-lat\]](#).
- [20] C. Alexandrou, A. Athenodorou, and K. Jansen, *Phys. Rev. D* **92**, 125014 (2015), [arXiv:1509.04259 \[hep-lat\]](#).
- [21] I. Horvath, S. J. Dong, T. Draper, F. X. Lee, K. F. Liu, H. B. Thacker, and J. B. Zhang, *Phys. Rev. D* **67**, 011501 (2003), [arXiv:hep-lat/0203027](#).
- [22] I. Horvath, A. Alexandru, J. B. Zhang, Y. Chen, S. J. Dong, T. Draper, K. F. Liu, N. Mathur, S. Tamhankar, and H. B. Thacker, *Phys. Lett. B* **617**, 49 (2005), [arXiv:hep-lat/0504005](#).
- [23] M. Lüscher, *JHEP* **08**, 071, [Erratum: *JHEP* 03, 092 (2014)], [arXiv:1006.4518 \[hep-lat\]](#).
- [24] M. Luscher and P. Weisz, *JHEP* **02**, 051, [arXiv:1101.0963 \[hep-th\]](#).
- [25] A. Chowdhury, A. Harindranath, and J. Maiti, *Phys. Rev. D* **91**, 074507 (2015), [arXiv:1409.6459 \[hep-lat\]](#).
- [26] J. Liang, Y.-B. Yang, T. Draper, M. Gong, and K.-F. Liu, *Phys. Rev. D* **98**, 074505 (2018), [arXiv:1806.08366 \[hep-ph\]](#).
- [27] S. Navas *et al.* (Particle Data Group), *Phys. Rev. D* **110**, 030001 (2024).
- [28] L. Gan, B. Kubis, E. Passemar, and S. Tulin, *Phys. Rept.* **945**, 1 (2022), [arXiv:2007.00664 \[hep-ph\]](#).
- [29] A. Alexandru, C. Pelissier, B. Gamari, and F. Lee, *J. Comput. Phys.* **231**, 1866 (2012), [arXiv:1103.5103 \[hep-lat\]](#).
- [30] A. Alexandru, M. Lujan, C. Pelissier, B. Gamari, and F. X. Lee, in *2011 Symposium on Application Accelerators in High-Performance Computing (SAAHPC'11)*, IEEE Nucl.Sci.Symp.Conf.Rec. (2011) pp. 123–130, [arXiv:1106.4964 \[hep-lat\]](#).